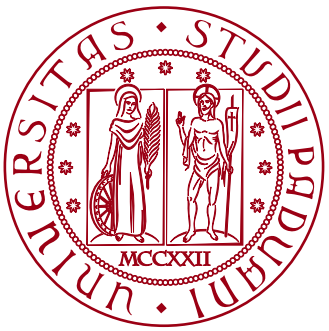

UNIVERSITÀ DEGLI STUDI DI PADOVA

Dipartimento di Fisica e Astronomia "Galileo Galilei"

Corso di Laurea in Fisica

Tesi di Laurea

Laser Absorption Spectroscopy Studies on the Caesium Ovens Test Stand

Relatore
Dr. Gianluigi Serianni
Correlatore
Dr. Marco Barbisan

Laureando
Leonardo Zampieri

Anno Accademico 2018/2019

Abstract

ITER, which is under construction in France, will be the largest and most ambitious experiment on thermonuclear controlled fusion. To reach the desired performances, additional heating systems will be needed: one of the most important will be the neutral beam injection (NBI). In particular, the technique consist in a negative ions source, followed by an acceleration system and a neutraliser, to produce a high-energy neutral beam; the beam collides with the ITER plasma particles, heating them. In the Neutral Beam Test Facility (NBTF) at Consorzio RFX in Padova SPIDER, a prototype of ITER NBIs, is under development. One of the key points of the system is the production of negative ions: to enhance the amount of ions produced inside the source, the inner walls will be covered with caesium. For this purpose, caesium will be vaporised inside the source. The ovens for caesium vaporisation and the diagnostics for caesium density monitoring are nowadays subjects of study. In particular, a Laser Absorption Spectroscopy diagnostic (LAS) will be installed: it will permit, using the D_2 caesium optical absorption line, the estimation of the average Cs density along different lines of sight. This is fundamental to control the distribution of the caesium vapours inside the source: peaks or lack of caesium can result in high efficiency drops, non uniformity in beam intensity and beam divergence, and operational problems, that can cause lack of supply in ITER.

To test the SPIDER caesium ovens, a test stand has been built: the CAesium ovens Test Stand, CATS. In the same test stand, a Laser Absorption Spectroscopy diagnostic is tested: during the work reported in this thesis, the optical system has been set up and calibrated, the absorption phenomena has been studied and the analysis algorithm has been improved. A particular attention has been payed to the source of systematic errors, such as saturation and depopulation: their entity has been detected, an experimental guideline to minimise them has been produced and an analysis method to correct them a posteriori has been partially successfully tested.

As final result, LAS has been used to characterise the first two SPIDER ovens: in particular, the caesium density around the oven nozzle has been proved to be dependent on the oven reservoir temperature, and measurements from the two tested ovens has been found compatible within about 25%.

Contents

Chapter 1

Introduction

1.1 Fusion for energy

Since the industrial revolution, one of the most important topic in scientific research is production, transportation and storage of energy. Global energy consumption increased by 3% in 2018, and the main sources are oil, gas and coal. There are several reasons to search for a new energy source. Firstly, fossil fuels are not an infinite resource: according to the R/P ratio[1], oil reserves will run out in 50 years, gas ones in 51 years and coal ones in 132 years. Secondly, the carbon emissions from energy use has increased by 2% in 2018: to keep the climatic balance of the earth, they must be reduced [3].

In 1919, thanks to a mass spectrometer, the English physicist F.W. Aston measured that helium mass is a bit less of four-times the hydrogen mass. This difference lead another English physicist, A. Eddington, to suppose sun and all stars take energy from nuclear fusion [6], and researchers started thinking how to reproduce nuclear fusion on a laboratory.

Since there, lots of steps has been done.

A explored way to achieve energy production from fusion is through deuterium and tritium reactions:

$$
\begin{aligned}
{}^2\mathrm{H} + {}^2\mathrm{H} &\xRightarrow{50\%} {}^3\mathrm{He} + \mathrm{n} \\
{}^2\mathrm{H} + {}^2\mathrm{H} &\xRightarrow{50\%} {}^3\mathrm{H} + {}^1\mathrm{H} \\
{}^2\mathrm{H} + {}^3\mathrm{H} &\Rightarrow {}^4\mathrm{He} + \mathrm{n} \\
{}^2\mathrm{H} + {}^3\mathrm{He} &\Rightarrow {}^4\mathrm{He} + {}^1\mathrm{H}
\end{aligned}
$$

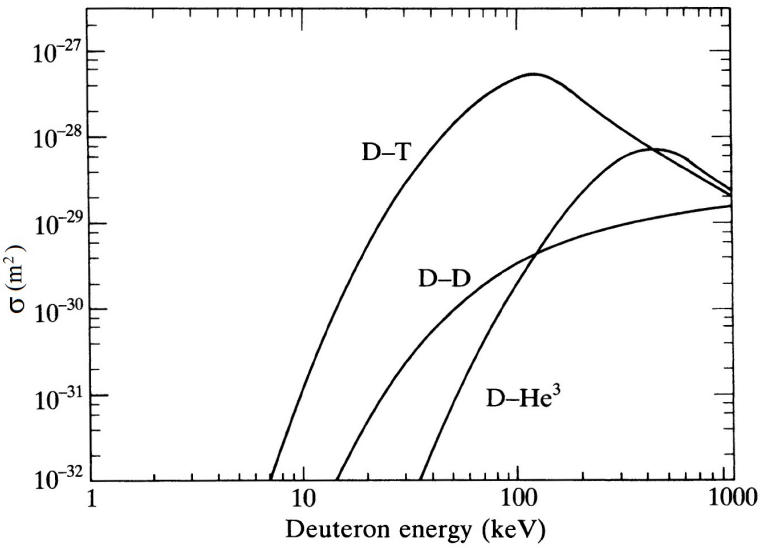

Figure 1.1: Cross section of various fusion reactions, as depending from deuterium atom energy, assuming the other atom is at rest. The $D - D$ curve shows the cumulative cross section of the two relative reactions

[1]Reserves-to-production ratio: the reserves remaining at the end of 2018 divided by the production in 2018, it provides an estimation of the length of time that those remaining reserves would last if production were to continue at that rate.

Fig. 1.1 shows the relation between cross sections of these reactions and energy of deuterium atom: it is clear that the reaction with highest cross section at lower energies is the $D-T$ one.

$$^{2}\mathrm{H} + {}^{3}\mathrm{H} = {}^{4}\mathrm{He}(3.5\mathrm{MeV}) + \mathrm{n}(14.1\mathrm{MeV})$$

This reaction produces a high-energetic neutron, whose energy can be absorbed by a shield and converted in heat and then electricity. Unfortunately, this reaction is not simple to achieve: in order to overcome the Coulomb barrier, temperatures around dozens of keV are needed. At that temperatures, deuterium and tritium are in plasma state, so a confinement system is needed. One of the explored system is magnetic confinement: thanks to a properly created magnetic field, plasma particles are kept in a toroidal bound and heated. Lots of studies are active to study both magnetic and alternative confinement systems, but the most ambitious one is ITER, an international collaboration that aim to achieve nuclear fusion in a magnetic-confined plasma thermonuclear reactor.

1.2 ITER

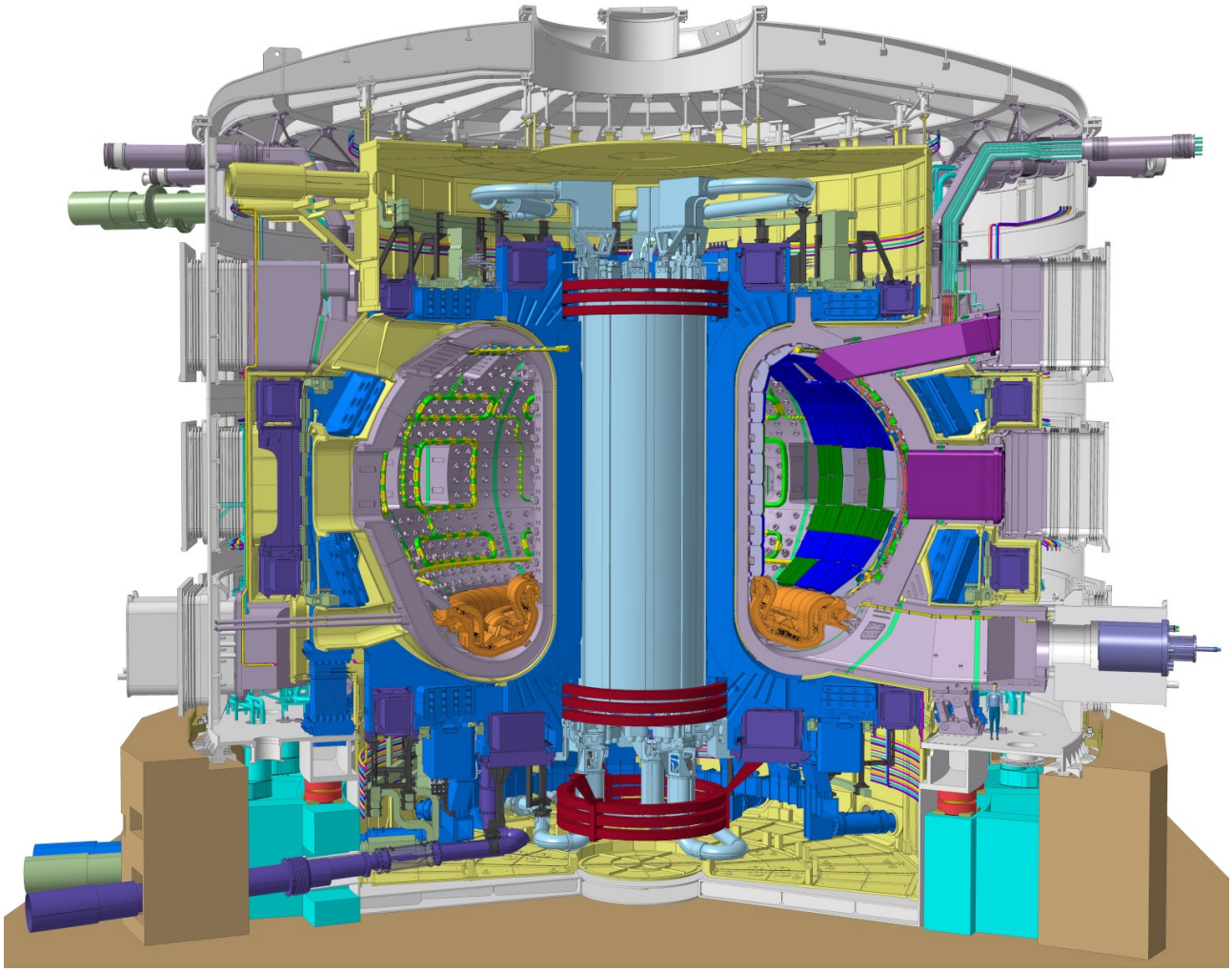

Figure 1.2: A cutaway of the ITER Tokamak [11]. The magnets can be seen in blue and light-blue, the divertors are orange, the external grey chamber is the cryostat while the toroidal internal one is the vacuum vessel. To understand the dimension of the machine, note the man in the bottom-right corner.

The ITER (International Thermonuclear Experimental Reactor, but also *way* in latin) project began in 1985 as the result of an agreement between European Union, Soviet Union, United States and Japan. Some years later, China, India and North Korea joined the project, and on 24$^{\mathrm{th}}$ October 2007 the ITER Organization came into existence. The main objective is to manage to build a working nuclear-fusion reactor, and prove that it can achieve a positive balance of energy. The parameters of the machine are shown in table 1.1, while the project of the machine can be seen in fig. 1.2.

Plasma volume	840m^3
Plasma major radius	6.2m
Plasma temperature	$150 \cdot 10^6\text{K}$
Plasma current	15MA
Plasma duration	$300 - 500\text{s}$
Magnet temperature	4K
Initial pressure	$\sim 0.1\text{Pa}$
Output power	500MW
Q	≥ 10

Table 1.1: Iter parameters. [12]

The machine aim to achieve a Q ratio (ratio between power extracted from the reactor and power required by the plant to work) of at least 10 (5 in stationary state). It also aim to merge all the necessary technologies in a unique device, and test modules and technologies for a future high-Q reactor.

To confine plasma in ITER a toroidal configuration has been chosen. In particular, the superconducting coils will produce a magnetic field in *tokamak* configuration. The plasma will be produced by a mixture of deuterium and tritium: the target is to reach a gain factor of ~ 10. To achieve this, gas must be heated to a temperature of 10keV to reach the plasma state and be able to overcome the Coulombian repulsion between nuclei. There are mainly three heating systems: ohmic heating ($P = RI^2$), given by the current carried by the plasma ions; RF heating, which consist in high frequency electromagnetic waves that resonate with plasma particles, and neutral beam injection (NBI). This last one consists in using a beam of high energy neutral hydrogen/deuterium atoms, which heat the plasma by colliding with its particles.

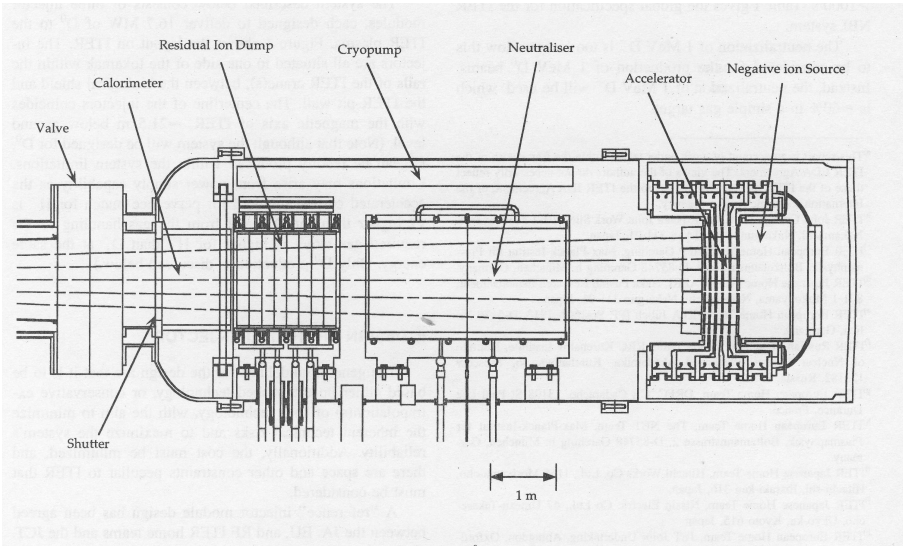

Figure 1.3: Scheme of the ITER neutral beam injector. [10]

Today, an efficient technique to accelerate neutral particles is not known: the most effective technique to produce a high-energy neutral beam consists in neutralizing an high-energy ion beam. The ITER neutral beam injector, as can be seen in fig. 1.3, will be made of the following elements:

Plasma source: 8 RF drivers produce an H/D plasma, which diffuses in a common expansion region;

Expansion chamber: plasma expands and ions are produced;

Accelerator: a system of grids at different electrostatic potentials extract ions from the source and accelerates them;

Neutraliser: a region filled of neutral gas induce a charge-exchange between ions, producing high-energetic neutrals;

Residual ion dump: a electrostatic or magnetic field removes residual ions from the beam.

Although injection system based on positive ions exists, for ITER a negative-ions injection system has been chosen. As can be seen from fig. 1.4, when beam energy increases the neutral fraction on a beam passed through

a neutraliser exponentially decreases for positive ions, while remains almost constant for negative ions: the ITER NBIs must supply a beam with particle energies of 1MeV, able to penetrate plasma and hit its particles, so a negative-ions system is the better choice.

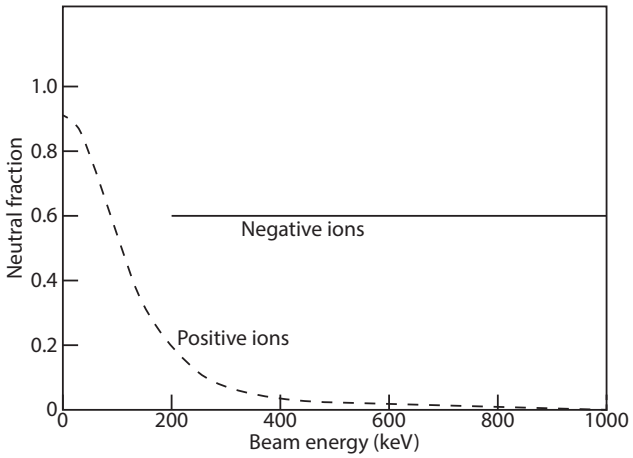

Figure 1.4: Neutral fraction on a beam passed through a neutraliser, for positive or negative ions [29].

Two neutral beam injectors —each one delivering a deuterium beam of 16.5MW with particle energies of 1MeV— are currently foreseen for ITER [12].

The beam injection system must be developed and tested: today, no NBI which reach all the performances required for ITER (as particles energy, beam power and current, divergence, efficiency and duration) at the same time exists. To do this, in Padova a Neutral Beam Test Facility (NBTF) has been built: it is a test facility for beam production and neutralisation, hosting two separate experiments: SPIDER and MITICA. SPIDER (Source for Production of Ions of Deuterium Extracted from Rf plasma) is the prototype for the negative ions sources, and aim to produce a 100keV ions beam and to prove the functionality of a 8-driver source. Moreover the source target parameters, as the beam uniformity and divergence and the ratio between extracted ions and coextracted electrons, are tested. MITICA (Megavolt ITER Injector & Concept Advancement), instead, will be the prototype of the whole system, producing a $1\text{MV} - 40\text{A}$ neutral beam. They both aim to reach a pulse length of 1h.

To produce negative ions, atoms shall capture an electron. There are two physical mechanisms responsible for this: volume production and surface production.

Volume production

The atom can capture an electron directly from the plasma: in particular, if a fast electron collide with a hydrogen molecule, the following reactions can happen [1]:

$$\mathrm{H_2} + \mathrm{e_{fast}} \Rightarrow \mathrm{H_2}^* + \mathrm{e} \Rightarrow \mathrm{H^-} + \mathrm{H_0}$$

where $\mathrm{H_2}^*$ represent a excited hydrogen molecule. Unfortunately, negative ions are affected by multiple process that can neutralise them: for example, mutual neutralisation ($\mathrm{H^-} + \mathrm{H^+} \Rightarrow 2\,\mathrm{H}$), associative detachment ($\mathrm{H^-} + \mathrm{H} \Rightarrow \mathrm{H_2} + \mathrm{e}$) or electron detachment ($\mathrm{H^-} + \mathrm{e} \Rightarrow \mathrm{H} + 2\,\mathrm{e}$, dominants at temperature $\geq$ 1eV). In negative ion sources a magnetic filter prevents high-energy electron to reach the extraction region, in order to reduce electron detachment and neutralisation and allow ions extraction. Unfortunately, with only volume production it is impossible to reach the ITER target flux parameters.

Surface production

The atom can capture an electron through the interaction with metal atoms on the walls of the plasma vessel. The process is called secondary negative emission: it is based on the tunnelling of an electron from the conduction band of the metal surface to an affinity level of an atom hitting the surface. The efficiency of the process strongly depends from the work function of the metal whose the surface is made of: if the work function of the surface is lowered, the Fermi level energy of the metal becomes comparable to the electron affinity of the atom and the tunnelling probability enhances.

To achieve this, a metal with low work function can be deposited on the surface: caesium is the element with lowest work function, so it has been chosen to be vaporised inside the plasma vessel. The work function of the surface reach a minimum with a caesium coverage of about 0.6 monolayers [4].

It is difficult to have a controlled deposition of caesium on the surface, and in plasma state caesium is continuously redistributed; moreover, caesium must be vaporised inside the source: ovens and relative diagnostics must be studied and tested. To achieve this, a CAesium ovens Test Stand (CATS) has been built.

1.3 Caesium Ovens and CATS

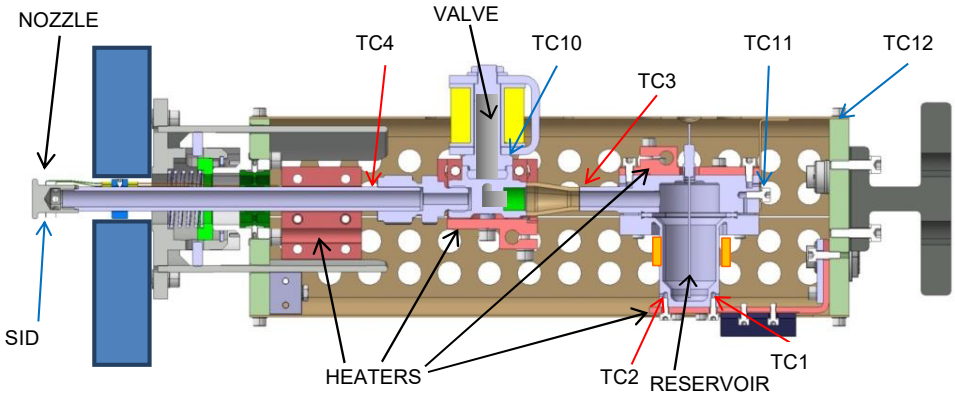

Figure 1.5: Oven structure and diagnostics positions

Caesium will be evaporated inside SPIDER using 3 ovens (figg. 1.5 and 1.6(a)). A reservoir contains the liquid caesium; a duct connects it to a solenoid valve, normally closed; after that, the duct ends in a nozzle, that permits the diffusion of caesium. Multiple heaters heat the caesium in the reservoir and along all the duct. Each oven is equipped with thermocouples that monitor the temperature in various points. In particular, TC4 measures the duct temperature, while TC1 and TC2 measures the reservoir one.

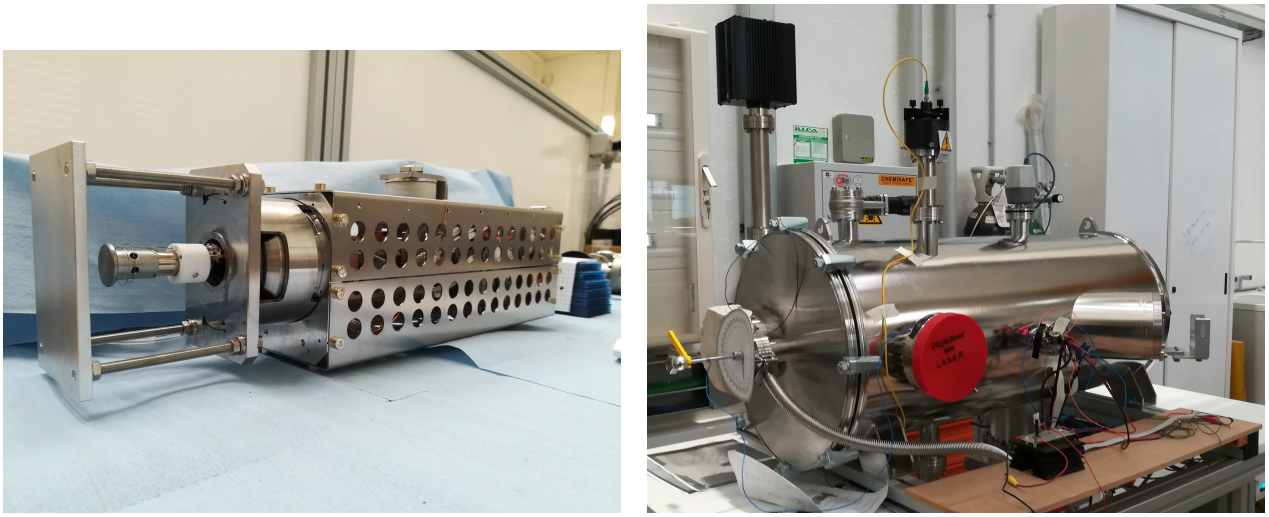

(a) A oven: in the foreground, the nozzle.

(b) CATS vacuum vessel, with all diagnostics

Figure 1.6: Pictures from CATS.

The ovens need to be tested and characterised: for this purpose, a specific test stand has been built: CATS (fig. 1.6(b)). It consists in a vacuum vessel, where the caesium oven is installed and it operates replicating the SPIDER conditions. The vessel is equipped with a pumping group, that can reach a base pressure of $5 \cdot 10^{-8}$mbar, compatible with the SPIDER base vacuum, and various diagnostics. All the sensors, diagnostics and switches are controllable via pc and all the collected data are registered in a MDSPlus server [15]. Between the diagnostics mounted on CATS, a (optional) thermal camera record the thermic oven profile from behind, and a residual gas analyser is available to detect impurities inside the vessel. Three different systems are available to detect the caesium density inside the vessel: two Surface Ionization Detectors (SID), one near the oven nozzle and the other mobile, and a Laser Absorption Diagnostic. This last diagnostic is planned also in SPIDER, with multiple line of sights: it has been reproduced in CATS to be tested. In particular, the systematic errors as

signal saturation and depopulation can be studied and their entity can be estimated, providing some correction factors.

This thesis will focus on Laser Absorption Spectroscopy, its measurements and its calibration. The purpose is to assemble, calibrate and operate a LAS diagnostic, analyse collected data and use them to characterise caesium ovens.

In the second chapter the absorption theory will be presented and the relation between intensity and density will be searched. In the third chapter, the experimental setup will be described and the calibration of the system will be reported. In the fourth chapter the analysis algorithm will be presented, and systematic errors (like saturation and depopulation) entities estimated. Finally, in the fifth chapter the results about the ovens characterisation will be reported.

Chapter 2

Laser Absorption Spectroscopy

2.1 Absorption theory

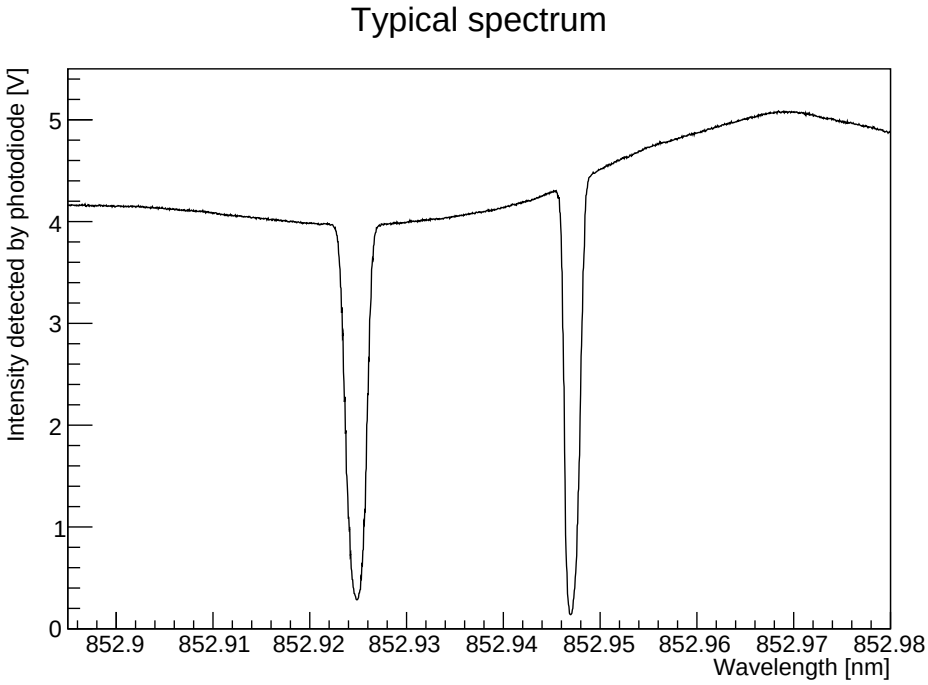

Figure 2.1: A typical absorption spectrum of the Cs D2 line: the intensity (as function of wavelength) shows the two clear absorption peaks. In the vertical axis the voltage detected by the photodiode, proportional to the beam intensity, is reported.

When a light beam passes through a medium of density n, some of the photons get absorbed by the atoms and the intensity of the beam is reduced (fig. 2.1). If the beam intensity is not too strong, the fraction of already-excited atoms can be neglected and so spontaneous and stimulated emission; only absorption can be considered. The intensity exponentially decreases with the medium depth (Beer Lambert law), and in particular:

$$\frac{\mathrm{d}I(\lambda, x)}{\mathrm{d}x} = -\sigma(\lambda) n(x) I(\lambda, x) \tag{2.1}$$

where $\sigma(\lambda)$ is the absorption cross section, λ the beam wavelength, $n(x)$ the atomic density and $I(\lambda, x)$ the beam intensity. Considering the density constant over x, the differential equation can be easily integrated over a path of generic length L:

$$I(\lambda, L) = I(\lambda, 0) e^{-\sigma(\lambda) n L} \tag{2.2}$$

Upon integrating with respect to λ, density can be written as a function of the other parameters:

$$\ln \frac{I(\lambda,0)}{I(\lambda,L)} = \sigma(\lambda) n L \tag{2.3}$$

$$\int \ln \frac{I(\lambda,0)}{I(\lambda,L)}\,\mathrm{d}\lambda = nL \int \sigma(\lambda)\,\mathrm{d}\lambda \tag{2.4}$$

$$n = \frac{1}{L}\frac{1}{\int \sigma(\lambda)\,\mathrm{d}\lambda} \int \ln \frac{I(\lambda,0)}{I(\lambda,L)}\,\mathrm{d}\lambda \tag{2.5}$$

It is useful to define the line profile function:

$$\bar{g}(\nu) \coloneqq \frac{\sigma(\nu)}{\overline{S}} \quad \text{st} \quad \int_{-\infty}^{+\infty} \bar{g}(\nu)\,\mathrm{d}\nu = 1 \tag{2.6}$$

where $\overline{S}$ is the mean oscillator strength and ν the beam frequency. For photon absorption, $\overline{S}$ can be written as a function of the Einstein coefficient A_{ik} [22]:

$$\overline{S} = \frac{\lambda_0^2}{8\pi}\frac{g_i}{g_k} A_{ik} \tag{2.7}$$

where λ_0 is the central absorption wavelength and g_i and g_k the statistical weights of respectively the ground level and the excited level . To substitute (2.6) into (2.5), the integral variable must be changed; remembering that $c = \lambda\nu$ (where c is the light speed):

$$\int \sigma(\lambda)\,\mathrm{d}\lambda = \int \sigma(\nu)\frac{\mathrm{d}\lambda}{\mathrm{d}\nu}\,\mathrm{d}\nu \tag{2.8}$$

$$= \int \sigma(\nu)\frac{c}{\nu^2}\,\mathrm{d}\nu \tag{2.9}$$

$$= \overline{S}\int \bar{g}(\nu)\frac{c}{\nu^2}\,\mathrm{d}\nu \tag{2.10}$$

Typically, the line width is way smaller than the central frequency ($\Delta\nu \ll \nu_0$): ν can be considered constant over the support of $\bar{g}$.

$$\int \sigma(\lambda)\,\mathrm{d}\lambda \approx \overline{S}\frac{c}{\nu_0^2}\int \bar{g}(\nu)\,\mathrm{d}\nu \tag{2.11}$$

$$n = \frac{1}{L}\frac{1}{\overline{S}\frac{c}{\nu_0^2}\underbrace{\int \bar{g}(\nu)\,\mathrm{d}\nu}_{1}} \int \ln \frac{I(\lambda,0)}{I(\lambda,L)}\,\mathrm{d}\lambda \tag{2.12}$$

$$= \frac{8\pi c}{\lambda_0^4}\frac{1}{L}\frac{g_k}{g_i A_{ik}} \int \ln \frac{I(\lambda,0)}{I(\lambda,L)}\,\mathrm{d}\lambda \tag{2.13}$$

Using this relation, the caesium density can be calculated from the intensity spectrum. This relation, however, is valid only for neutral atoms at ground state. In the test stand the caesium gas is mainly in the ground state, but in SPIDER the caesium will be also in contact with plasma and so partially ionised: the obtained value will refer only to the density of the neutral caesium, and should be rescaled to consider ionisation.

This last equation shows that the value of n depends only from the ratio between intensities: this suggests that, if there is no signal offset, the intensity does not need to be calibrated.

2.2 Line profile

It will be useful to calculate the line profile function, $\bar{g}(\nu)$, to understand its shape. The Doppler broadening of the line can be assumed way larger than the natural line width: this assumption will be verified later (eq. (2.32)).

Due to Doppler effect, the centre of the line profile becomes:

$$\nu_0 = \nu_0^* \left(1 + \frac{v}{c}\right) \tag{2.14}$$

Where ν_0 is the observed central wavelength, and ν_0^* is the true central wavelength, with the medium at rest.

Let's consider a hot gas in thermal equilibrium, and the particle speeds following a Maxwell distribution. The probability density function of the particle speed around an axis is [5]:

$$p(v) = Ae^{-\left(\frac{v}{v_P}\right)^2} \tag{2.15}$$

$$\text{where } v_P = \sqrt{\frac{2kT}{m}} \tag{2.16}$$

where v_P is the most probable speed, k the Boltzmann constant, T the temperature, m the mass of the gas particles and A the normalization factor.

The resulting line profile $\bar{g}$ is the convolution of the natural line profile g with the speed PDF:

$$\bar{g}(\nu) = \int g_{\nu_0(v)}(\nu) p(v)\,\mathrm{d}v \tag{2.17}$$

where $g_{\nu_0(v)}$ is the natural line profile centred in $\nu_0(v)$. Doppler broadening is assumed way larger than normal line width: we can consider $g_{\nu_0(v)}(\nu) \approx \delta(\nu - \nu_0)$.

$$\bar{g}(\nu) = \int \delta(\nu - \nu_0(v)) p(v)\,\mathrm{d}v \tag{2.18}$$

$$= \int \delta\left(\nu - \nu_0^*\left(1 + \frac{v}{c}\right)\right) p(v)\,\mathrm{d}v \tag{2.19}$$

$$= p\left(c\frac{\nu - \nu_0^*}{\nu_0^*}\right) \tag{2.20}$$

$$\sim \exp\left(-\left(c\frac{\nu - \nu_0^*}{\nu_0^* v_P}\right)^2\right) \tag{2.21}$$

Defining $\nu_P \coloneqq \frac{\nu_0^* v_P}{c} = \frac{\nu_0^*}{c}\sqrt{\frac{2kT}{m}}$ and forcing $\int \bar{g}(\nu)\,\mathrm{d}\nu = 1$:

$$\bar{g}(\nu) = \frac{1}{\nu_P\sqrt{\pi}} e^{-\left(\frac{\nu-\nu_0}{\nu_P}\right)^2} \tag{2.22}$$

that is a Gaussian profile. This result is very useful because it allows to fit collected data with a Gaussian, removing some of the data noise.

2.3 Depopulation

In the derivation of the previous relations, the fraction of already-excited atoms and the spontaneous and stimulated emission have been neglected. During the experimentation in CATS this approximation is not always valid: if Cs density is low and laser beam is intense, a non-negligible fraction of caesium atoms are already excited and can not absorb another photon. Besides, these atoms will relax emitting a photon.

In the study of line broadening, an important classification must be done: if the probability of absorption or emission of radiation is equal for all the particles of a sample that are in the same energetic level, the broadening is called *homogeneous*; otherwise, it is called *inhomogeneous*. When the Doppler effect is not negligible, the probability depends on the velocity of each particle, so inhomogeneous broadening relations must be used.

The new line profile can be written in a Lorentzian shape, and the combination of Doppler broadening and population inversion lead to increase of the FWHM. As a result, the attenuation factor is reduced by intensity-dependent value [5]:

$$\frac{\mathrm{d}I(\lambda, x)}{\mathrm{d}x} = -\frac{I(\lambda, x)}{\sqrt{1 + \beta I(\lambda, x)}}\sigma(\lambda) n \tag{2.23}$$

where

$$\beta = \frac{g_k}{g_i}\frac{2\sigma_0\lambda_0}{hcA_{ik}} \tag{2.24}$$

with σ_0 the resonant cross section, λ_0 the central absorption wavelength and h the Plank constant.

Assuming the density constant over the beam path, the differential equation can be integrated:

$$\int_0^L \frac{\sqrt{1+\beta I}}{I}\,\mathrm{d}I = -\int_0^L \sigma(\lambda) n\,\mathrm{d}x \tag{2.25}$$

$$\sigma(\lambda) n L = \left[2\sqrt{1+\beta I} + \ln\frac{\sqrt{1+\beta I} - 1}{\sqrt{1+\beta I} + 1}\right]_L^0 \tag{2.26}$$

The new relation for n becomes:

$$n = \frac{8\pi c}{\lambda_0^4}\frac{1}{L}\frac{g_k}{g_i A_{ik}}\int\left[2\sqrt{1+\beta I} + \ln\frac{\sqrt{1+\beta I}-1}{\sqrt{1+\beta I}+1}\right|_L^0 \mathrm{d}\lambda \tag{2.27}$$

This equation is better than (2.13) when the depopulation effect can not be neglected. However, it is simple to show, using Taylor expansions, that for small I the two relations are equivalent. On the other hand, this second relation needs the spectrum signal to be correctly calibrated in intensity, and this introduces a source of systematic error.

2.4 Caesium proprieties

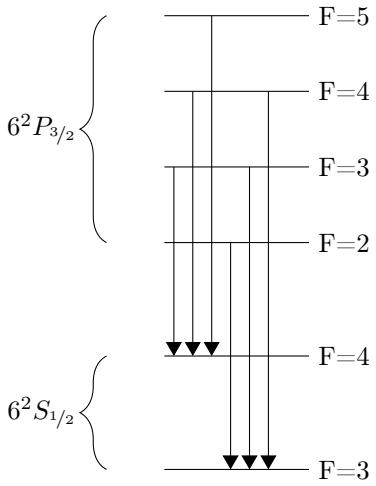

Figure 2.2: Hyperfine structure for caesium D2 line

The ground state of caesium is $6^2S_{1/2}$, while the first excited state splits in two terms, $6^2P_{1/2}$ and $6^2P_{3/2}$. The respective transitions are called $D1$ (895nm) and $D2$ (852nm), respectively [23, 14]. The second one is more suitable for laser absorption spectroscopy, due to its low wavelength, for which detector and laser have a better resolution. This emission line splits in 6 levels due to hyperfine structure, as can be seen in figure 2.2.

$$g_i = 4 \qquad g_k = 2 \tag{2.28}$$

$$\lambda_0 = 852.34727582(27)\text{nm} \tag{2.29}$$

$$A_{ik} = 3.2889(84)\cdot 10^6 \text{s}^{-1} \tag{2.30}$$

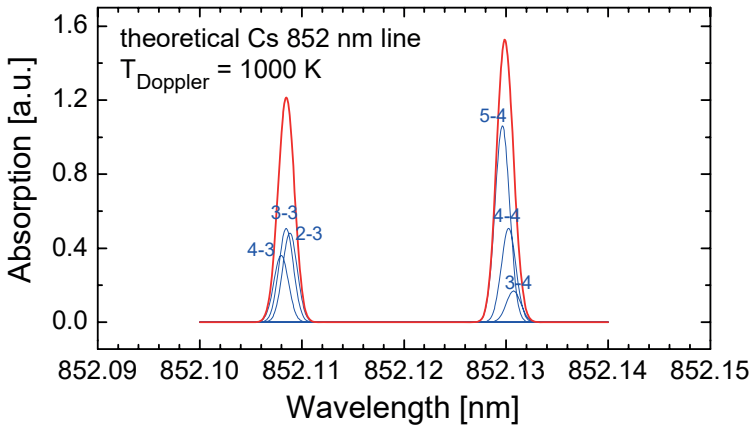

Figure 2.3: Doppler broadening at 1000K and hyperfine structure for caesium D2 line [8]

Due to Doppler broadening, the hyperfine structure of $6^2S_{1/2}$ is not visible (figure 2.3), so it can be seen only the splitting due to the hyperfine structure of $6^2P_{3/2}$, that is:

$$\Delta\lambda = (21.8 \pm 0.2)\text{pm} \tag{2.31}$$

We can now verify that the Doppler broadening is, as supposed, larger than the natural line width:

$$\left.\begin{aligned}&\mathrm{FWHM}_\nu^{\mathrm{natural}} = 5.23\mathrm{MHz}\\&\mathrm{FWHM}_\nu^{400\mathrm{K}} = 2\sqrt{2\ln 2}\frac{\nu_P}{\sqrt{2}} \approx 437\mathrm{MHz}\end{aligned}\right\} \mathrm{FWHM}_\nu^{\mathrm{natural}} \ll \mathrm{FWHM}_\nu^{400\mathrm{K}} \tag{2.32}$$

The resonant cross section is also tabulated (the tabulated value is valid for π-polarized light; as first approximation, is valid even for the considered case):

$$\sigma_0 = 2.3125082043(10) \cdot 10^{-13}\mathrm{m}^2 \tag{2.33}$$

$$\beta = \frac{g_k}{g_i}\frac{2\sigma_0\lambda_0}{hcA_{ik}} = (0.302 \pm 0.001)\mathrm{m}^2\,\mathrm{W}^{-1} \tag{2.34}$$

The overlapping of the hyperfine spectral levels force to work with the two visible lines, that are sums of multiple lines; this can lead to small deviations in the estimation of the density. Moreover, the different hyperfine levels does not depopulate in the same way: to make a precise depopulation correction, each level should be studied separately and the difference between the relaxation paths should be taken in account. Unfortunately, the overlapping of the levels obstruct a precise calculation, so the depopulation correction is only approximative.

Chapter 3

Experimental setup and calibration

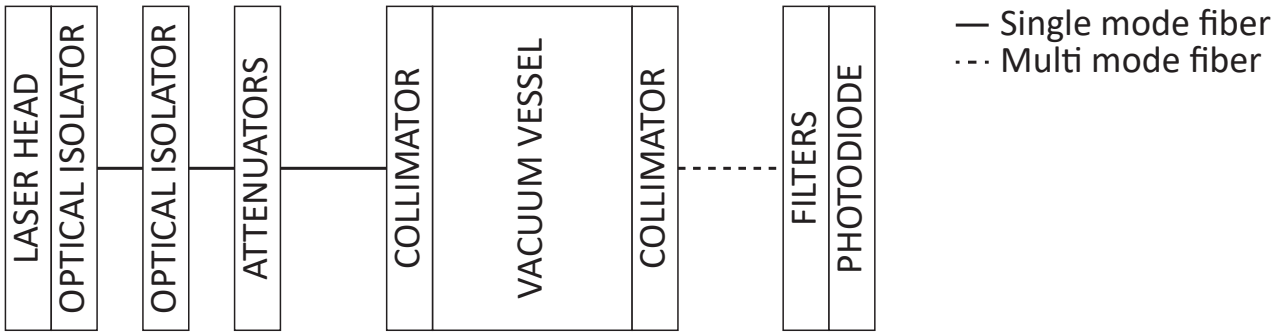

Figure 3.1: Laser beam path

As shown in fig. 3.1, the laser beam follows a light path from the diode to the photodiode passing through the vacuum vessel, in which there is caesium of unknown density. Multiple optical isolators prevent the laser head from damaging, while attenuators and filters permit online regulation of the laser intensity. (Models and characteristics of the components come from [2].)

3.1 Laser

The laser dedicated to LAS diagnostic is a 3B-class laser diode of central wavelength 852nm (Model DFB-0852-150-TO3, purchased from *Sacher Lasertechnik* [21]). The diode is hosted in a laser head (LH-Cheetah), equipped with an optical isolator (ISO-35-0850-4, 35dB isolation 92% transmission, 4mm clear aperture) and a fibre connector, and is powered and regulated by a dedicated controller (PilotPC 500). This has a feedback system to keep the temperature of the laser constant (28.96°C), and allows to set and/or modulate the laser current; this quantity linearly influences both the laser power and the laser wavelength. The controller can be remotely regulated and produces a monitor signal for the laser current. The laser current-wavelength coefficient specified by the manufacturer is:

$$\frac{\mathrm{d}\lambda}{\mathrm{d}I} = 0.003\mathrm{nm\,mA^{-1}} \tag{3.1}$$

The laser head must be carefully coupled to the fibre, to extract as much power as possible. Connecting the output fibre to a power meter (*Thorlabs* PM100D, S121C and S130C [24]) and iterating the rotation of the six screws on the laser head, the position that maximises the output power has been set.

3.2 Optical path

Downstream the laser head, an extra optical isolator (*Thorlabs* IO-F-850APC, 36dB isolation [25]) has been added, to prevent back-reflected light from reaching and damaging the laser diode. Then, two attenuators continue the optical line. In the first experimental campaign a variable fibre attenuator (*Thorlabs* V800A [26]), whose attenuation can be controlled by a voltage signal supplied by the pc control system, and a manually adjustable fibre attenuator (*OZ Optics* BB-500-11-850-5/125-S-50-3A3A-3-1 [19]) have been used. Some tests on the second one, whose attenuation can be manually regulated by means of a screw, have highlighted a lack of reproducibility: to avoid systematic errors, the attenuation has been regulated on the system setup and has

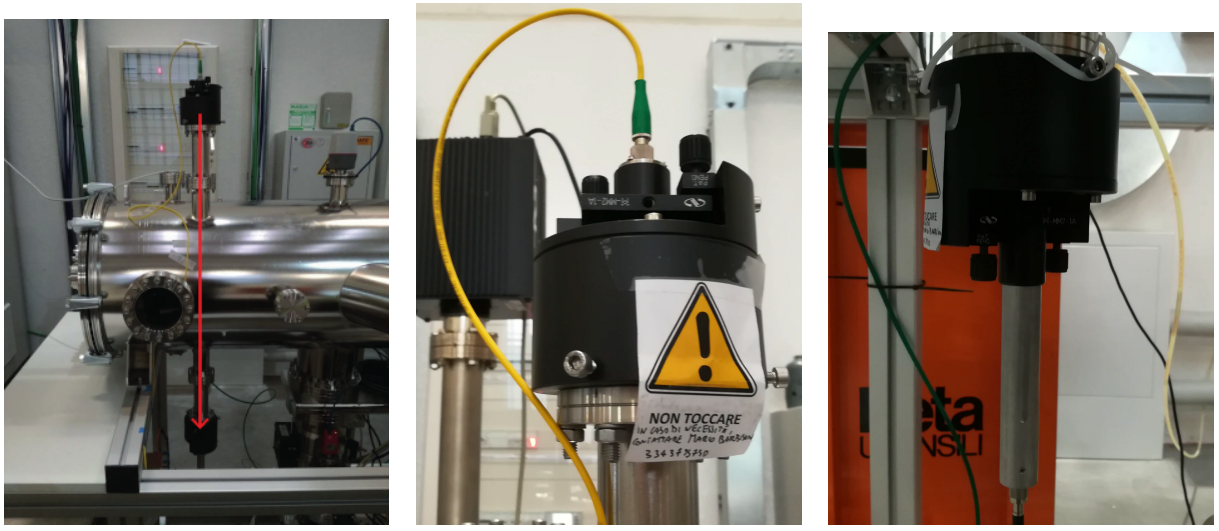

(a) Light path inside the vacuum vessel (b) Transmission collimator (c) Reception collimator

Figure 3.2: Light beam through vacuum vessel.

been kept fixed during the experimental campaign. During the second experimental campaign, the permanent attenuator has been replaced by a variable attenuator similar to the first one. All the components have been connected with their included fibres, using where needed *Thorlabs* ADAFC4 mating sleeves [27]. To calibrate attenuators, each one has been connected to the laser head and, on the other side, to a power meter: measuring the light intensity at different supplied voltages, the transfer functions have been obtained (fig.3.3).

A *OZ Optics* [20] 5µm-core 125µm-cladding single mode fibre leads the light to the vacuum vessel. It has two windows dedicated for the LAS: they are kept away from the oven nozzle to prevent glass opacification due to caesium deposition. Through a collimator, the beam changes propagation medium: from the fibre to air. The free beam passes through the first window, travels across the vacuum vessel and reaches the second window: just downstream of it, another collimator catches the beam into another fibre (fig. 3.2).

The collimators are equipped with fibre connectors and lens, and mounted on a structure with 2 translational degrees of freedom and 2 tilting screws. This allows to align the two collimators, having the beam almost totally collected by the second one: they have been regulated to maximise the recollected power. The beam produced by the transmission collimator has been measured by previous tests 6.5mm width [2].

After the second collimator, a multi mode fibre (1mm-core 1.1mm-cladding) leads the light to a photodiode. The higher core diameter was chosen to couple as much light as possible in the fibre.

Vessel path length

To compute the density, the length of the path is needed. The most realistic assumption is that the caesium atoms follow a straight path from the nozzle, and the density is uniform along the line of sight. This is not true, but it leads to an average value of the density along the line of sight. The interesting portion of the beam path is the red one in the figure 3.4. Therefore it can be calculated:

$$l = 482\text{mm} \tag{3.2}$$

3.3 Photodiodes

The beam is finally received by a photodiode (*OSI* OSI020-UV [18]), which converts it to a voltage signal proportional to the received power. Each photodiode is hosted in a custom module, which couples it to a programmable gain amplifier. The amplification factor can be set both locally (by means of a dip switch) and remotely (by means of a pc interface, not used): the available amplification values are $0x$ (all off), $10x$ (first switch on), $100x$ (second switch on) or $1000x$ (all switch on, never used). The fibre is coupled to the photodiode thanks to an aspheric condenser lens (*Thorlabs* ACL108U [28]), which collimates the light beam to the sensitive area of the photodiode. An optional interference filter is inserted between the lens and the photodiode, to measure only a narrow range of wavelengths centred on the D2 caesium line. Four different photodiodes (fig. 3.5), each with a setup optimal for a different range of intensities, have been prepared: two with and without the interference filter, and two with both interference filter and intensity filter. The intensity filters are needed to reduce the intensity and prevent photodiode damage, allowing measurements with high laser intensity; neutral

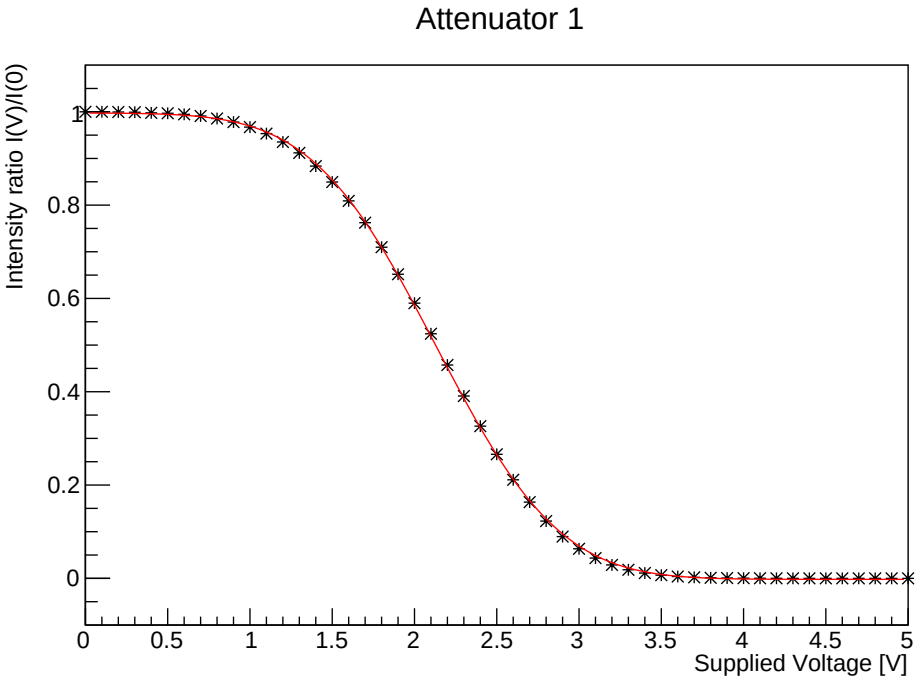

(a) Attenuator 1.

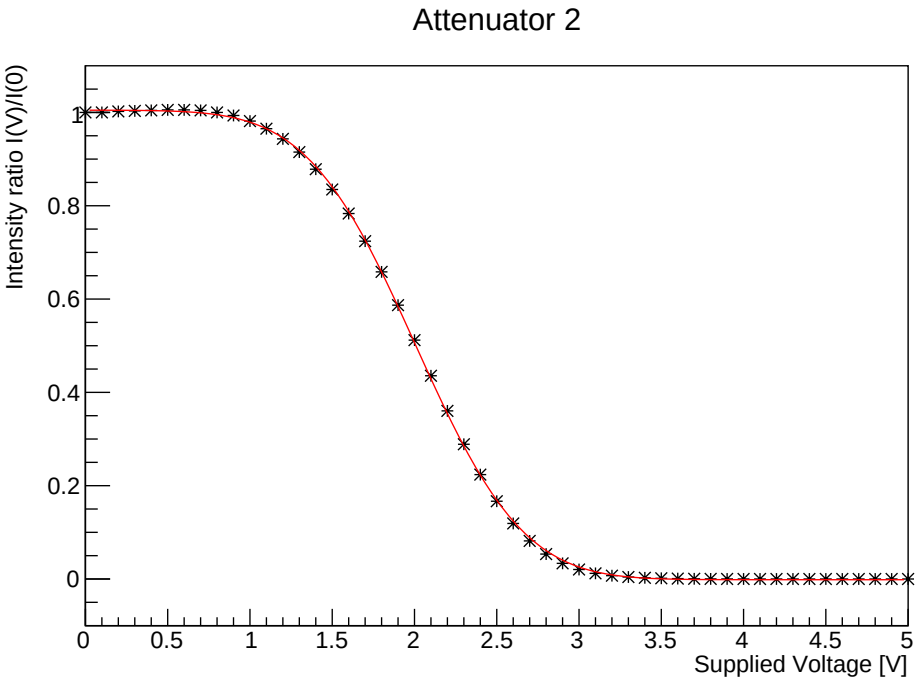

(b) Attenuator 2.

Figure 3.3: Power measured downstream the attenuator as function of supplied voltage, normalised to the value at 0V, and trend.

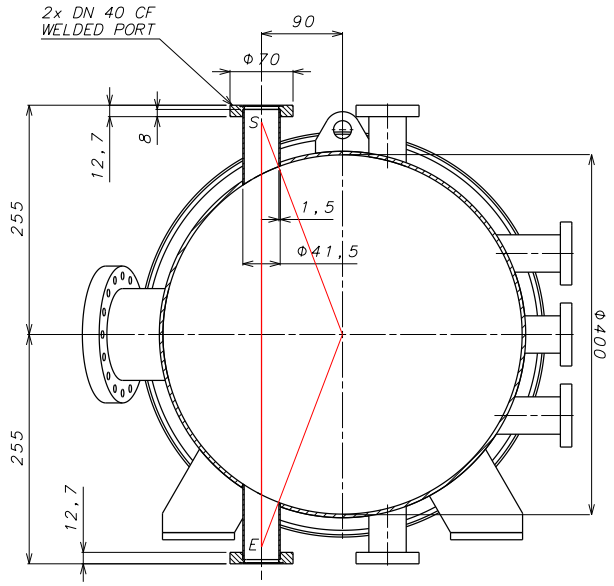

Figure 3.4: Section of the vessel: the red vertical line represent the portion of beam path considered for density computation. Data in millimetres.

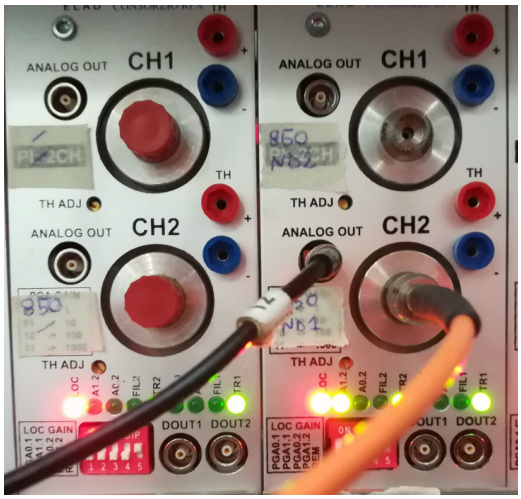

Figure 3.5: The four prepared photodiodes.

density ND filters, i.e. filters that reduce light intensity uniformly in each wavelength, with an optical density of 1 or 2 has been used. In the experimental campaigns presented here, only the *interference filter + ND1* photodiode has been used. The voltage signal produced by the photodiode is then acquired.

3.4 PC acquisition

The analog signal produced by photodiode, the laser current feedback signal and the attenuators voltage feedback signal are acquired by a *National Instruments* PXIe-6259 module [16], interfaced through a 2090-A 22 BNC connector block [17]. The same module produces the signals to modulate laser current and controls attenuators. The module has a 1.25MS/s multiplex acquisition rate, and can be set through the MDSplus software, which provide also for data storage [15].

3.5 Unexpected baseline oscillations

An unexpected phenomenon was revealed during the characterisation of the system. The photodiode signal is not linear with respect to the power emitted from the laser, but it is affected by oscillations (fig. 3.6). Using a power meter, the source of these oscillations was searched; the power was measured in different points of the light path and it was found that they are introduced in passing through the vacuum vessel. Downstream of

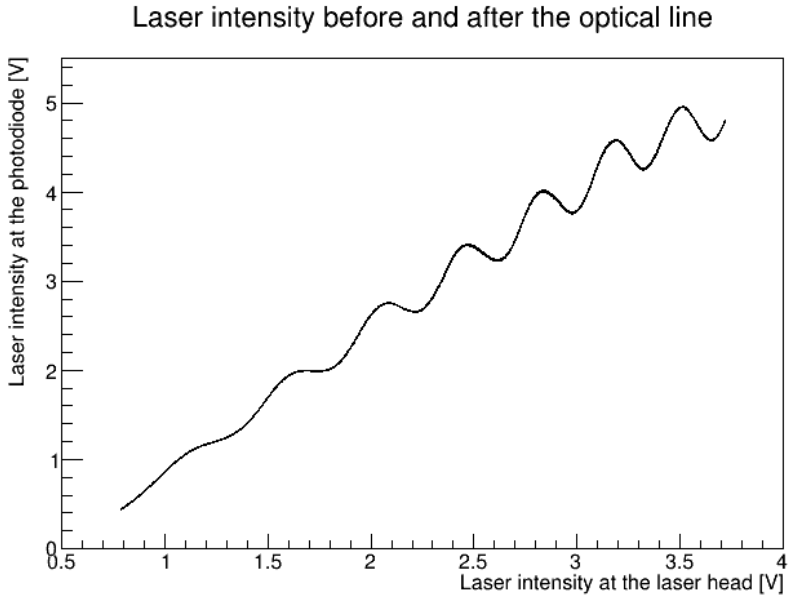

Figure 3.6: Power revealed from the photodiode as function of the power produced from the laser, with light travelling across the complete path. Both axis report a quantity, in Volts, linearly proportional to the beam intensity; the two measurements are not made with the same device, so calibration factors are different.

the transmission collimator, in fact, there are no oscillations, and upstream of the reception one they appear. Using the attenuators and comparing signals at different intensity, the oscillations have been proven to be wavelength-dependent (maximums and minimums appear at fixed wavelength).

Actually, this phenomenon is not clear. The oscillation has not a constant frequency along the wavelength spectrum: their period varies between 50pm and 100pm. It becomes smaller with the wavelength, contrary to all interference and diffraction phenomena. The refractive index of the windows (Kodial) is well measured in literature [13] and it does not apparentely present any non-linearity phenomena. The best remaining hypothesis is that there are some reflections done by the light inside the vessel, but no further details have been found.

However, the measurements are done in a very small portion of the spectrum, so these oscillations can be corrected using high-degree polinomial to interpolate the background signal.

3.6 Photodiode calibration

The photodiodes must be calibrated: the zero of the intensity must be fixed and, to use eq. (4.4), a relation between the intensity passing through the vessel and the voltage measured by the photodiode is needed. The calibration has been done only for the used photodiode, and results in different steps. Firstly, the background signal has been measured with the laser powered off: it results (-0.004 ± 0.001)V (Also, (-0.007 ± 0.002)V with $10x$ amplification and (-0.032 ± 0.002)V for $100x$ amplification). Secondly, the intensity has been measured with a power meter just upstream the reception collimator (the power meter is larger than the beam, so it is reasonable to assume it catches all the beam power, that is converted into intensity using the beam dimensions) as a function of the laser current, and then the photodiode signal has been recorded in the same laser current range. Comparing the power meter measurements with the photodiode ones at the same laser current, a voltage-intensity transfer function has been written (fig. 3.7).

$$I_{\text{after}} = mV + q \tag{3.3}$$

$$m = (3.62 \pm 0.03)\,\text{W m}^{-2}\,\text{V}^{-1} \tag{3.4}$$

$$q = (0.015 \pm 0.004)\,\text{W m}^{-2} \tag{3.5}$$

It is interesting to see the comparison plot (fig. 3.7): for the highest intensities, the oscillations cited above produce noise. This is due to the laser drift: the two compared measurements have been made some minutes one after the other; in this time, the laser had a wavelength drift and the maximums and the minimums of the oscillations moved. So, to make a better fit, only the lowest part of the graph is considered.

This relation allows to compute the intensity just downstream the vacuum vessel. To compute the intensity inside the vacuum vessel, the window contribution shall be considered. Some measures of the intensity are

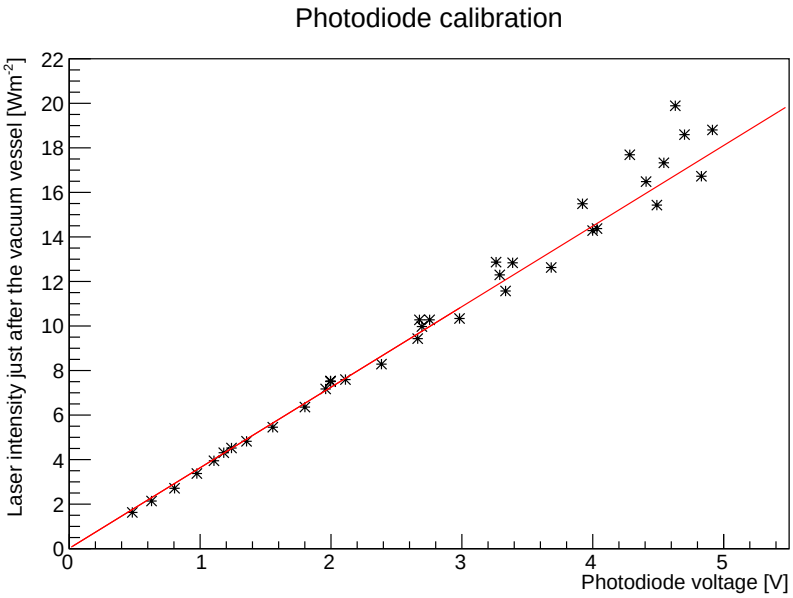

Figure 3.7: Voltage detected by the photodiode as a function of the intensity revealed from the power meter just after the vacuum vessel.

performed just upstream and just downstream the vacuum vessel: their ratio results $(82.8 \pm 0.7)\%$, stable at different intensities. Assuming the intensity is lowered only by the windows, we can affirm that each window reduces the power by a ratio of $\sqrt{82.8\%}$:

$$I_{\text{after}} = (91.0 \pm 0.4)\% I_{\text{inside}} \tag{3.6}$$

Finally, the analog amplification of the photodiode should be taken in account: the transfer function to convert the amplified signal to an equivalent signal (the voltage that would have been read if the amplification had let off) is computed by comparing some measurements of the same signals (background included) in different amplification conditions; what has been obtained is:

$$V^{\text{eq}} = mV + q \tag{3.7}$$

$$m^{10x} = (0.0996 \pm 0.0006) \qquad q^{10x} = (0.002 \pm 0.006)\text{V} \tag{3.8}$$

$$m^{100x} = (0.00996 \pm 0.00008) \qquad q^{100x} = (0.002 \pm 0.006)\text{V} \tag{3.9}$$

Chapter 4

Data collection and analysis

4.1 Analysis algorithm

An algorithm for the analysis already existed; the code, however, has been upgraded and improved. The analysis process is the following (fig. 4.1):

- The data are firstly downloaded from MDSplus data server;
- The peaks on the laser current modulation signal are searched for, and the signal is divided in segments; each segment corresponds to a single wavelength scan (fig. 4.1(a));
- An offset is applied to the photodiode signal, to make sure that it is directly proportional to intensity (see sec. 3.6);
- Then, for each segment, the photodiode signal is fitted via 8-degree polynomial (red line, fig. 4.1(a)). The residuals are computed and the negative peaks are found: the two highest ones are the sought absorption peaks (red stars, fig. 4.1(a));
- The photodiode signal is fitted again (blue line, fig. 4.1(a)), excluding a portion around the peaks identified in the previous step (green intervals, fig. 4.1(a)). The resulting polynomial is the background;
- The logarithm of the ratio between the background (just fitted polynomial) and the signal (measured data) is computed for each abscissa, to apply the relation (2.13) (fig. 4.1(b));
- The two peaks are fitted by Gaussians curves, as found in the relation (2.22) (red lines, fig. 4.1(b));
- The x axis is calibrated in wavelength using the known distance (eq. (2.31)) between the peaks;
- The integral is computed, and density is calculated using equation 2.13;
- The results, the fit parameters and all the settings used for the analysis are saved in MDSplus.

After the last improvements, the script is able to work online during data acquisition: data are saved to the server by the board every 10 seconds; the program downloads raw data from the server, computes density and uploads results to the server, allowing to have an immediate feedback of what is going on and check the operativity of the diagnostic.

Some tests have been done to verify the algorithm; in particular,

- Various fitting algorithms have been tested;
- Various fit guess parameters have been tried, for all the fits.

The tests showed that the algorithm is perfectly stable over these changes.

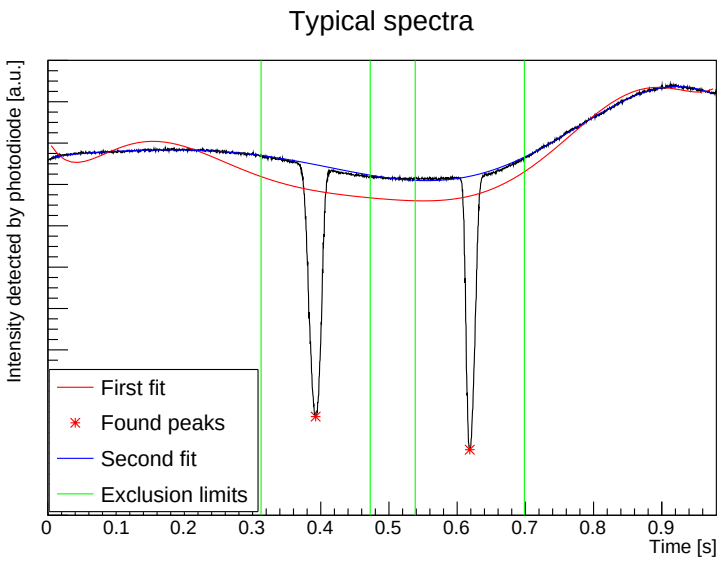

(a) First fit, peaks finding and second fit

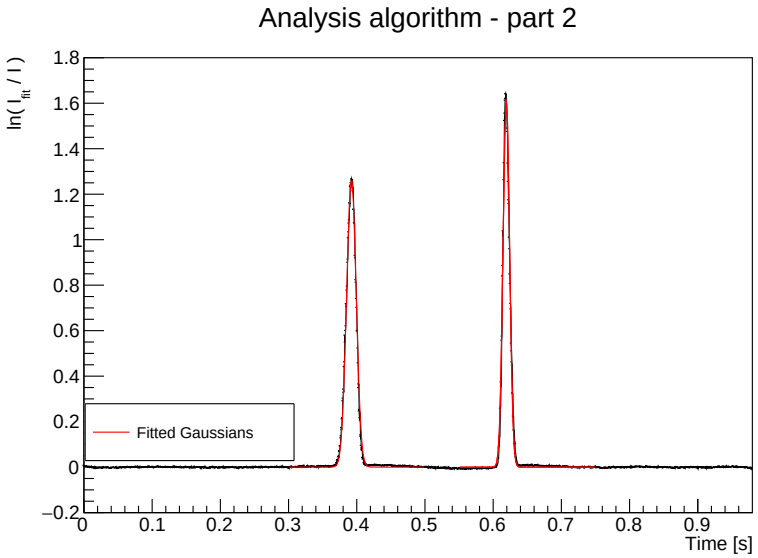

(b) Gaussians fit

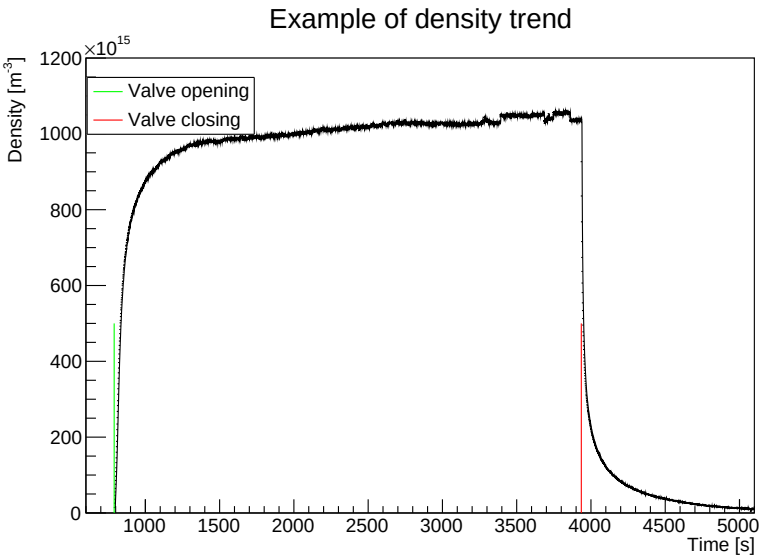

(c) Example of the density computed

Figure 4.1: Analysis method.

4.2 Saturation

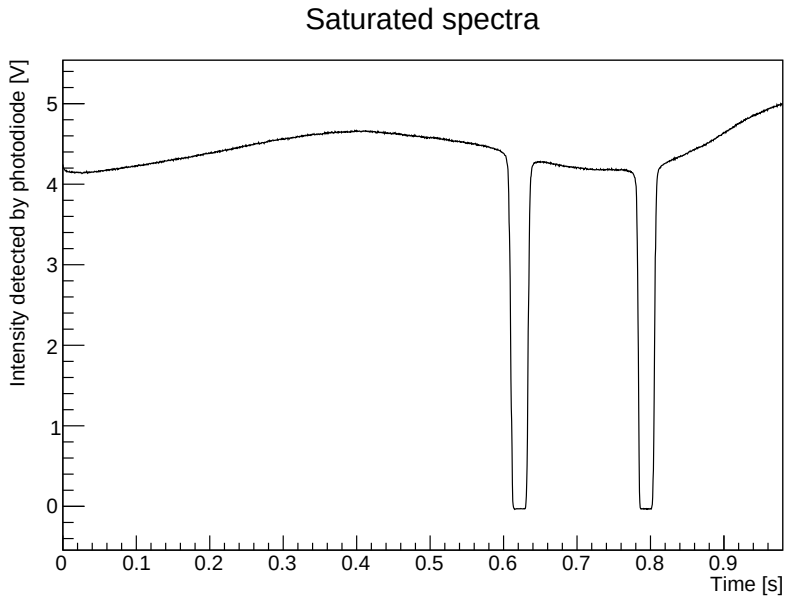

(a) Example of saturated signal. In the vertical axis the voltage measured from the photodiode, proportional to the intensity, is reported.

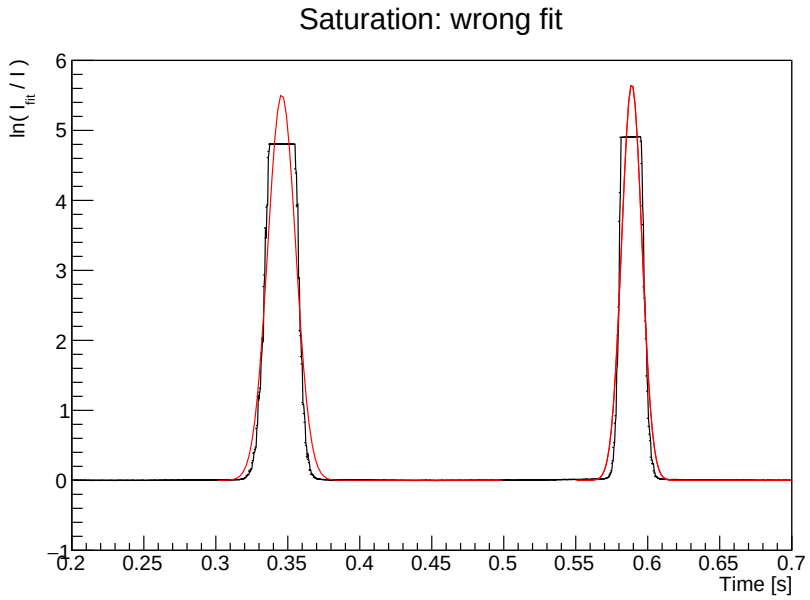

(b) Example of a wrong fit, due to saturation.

Figure 4.2: Saturation.

Two phenomena can distort density estimations: saturation and depopulation. The first one happens with high caesium densities and low laser intensities: if the laser beam is too weak, the signal gets saturated and some of the assumptions done in chap. 2 become false. The broad intrinsic baseline of the laser emission introduces an offset, that in the case of saturated spectrum becomes not negligible; in addition, the computation of the logarithm magnifies the offset error. Moreover, with saturated spectrum the line width of the laser line should be taken in account and the transmitted intensity goes near the photodiode detection limit [8].

To prevent wrong density calculation (as in fig. 4.2), a threshold shall be fixed and all data points below the threshold shall be ignored. Fitting only the Gaussian wings, saturation errors are avioded.

To choose the best threshold value, some tests have been done; a set of saturated signals has been randomly selected and the density has been computed with different threshold levels. The results are shown in fig. 4.3. The magnitude of the phenomena is clear: a low threshold causes a wrong fit that can change the computed value up to a factor of 5. On the other hand, a high threshold leads to a lack-of-data and unstable fits. As can

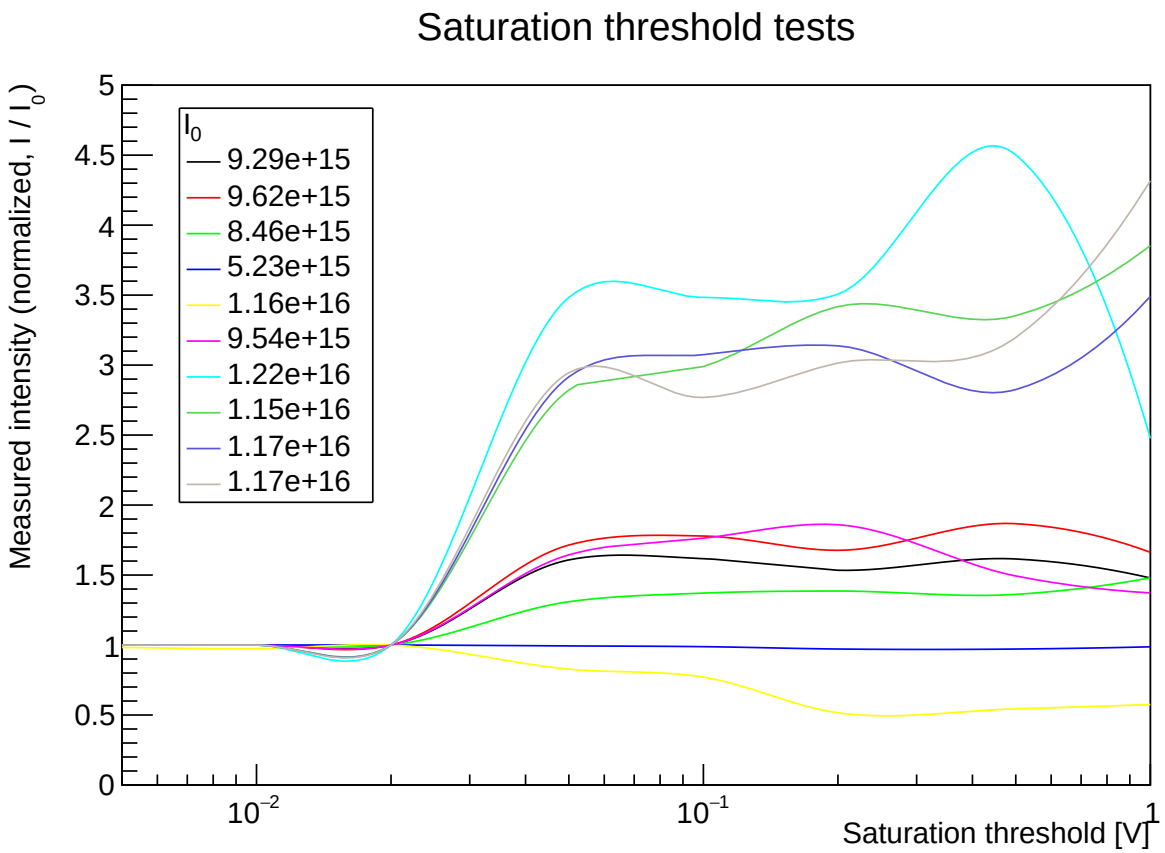

Figure 4.3: Tests on saturation threshold: density computed using different saturation threshold.

be seen from the graph, the stability zone is between 0.005 and 0.02V: to choose the better value the fit graphs has been analysed and, in the end, 0.005V is chosen.

4.3 Depopulation

A non-negligible systematic effect on density measurements is due to depopulation. When the laser intensity is too high in relation to the absorption medium, the fraction of already-excited atoms and the secondary emission can not be neglected: otherwise, density is underestimated. To consider depopulation, some tests have been done. Once the oven was in a stationary state (measured density constant over time), the attenuation has been lowered and measurements at different laser intensities have been made: the density has been then computed using both eq. (2.13) and (2.27). Some measures have been made with the oven in a non-perfectly stationary state: to be sure the density variations do not affect our results, before and after the attenuation scans density is measured at fixed attenuation; these data are then fitted with a third-degree polynomial and all the measures are rescaled to make the expected density constant.

To compute density using eq. (2.27), the laser intensity is needed; the use of the calibration equations (3.3) and (3.7) unavoidably introduces some errors, especially on the lower intensities when both photodiode-amplification rescaling and voltage-intensity conversion must be done.

The results are shown in figure 4.4: dots of the same colour are collected with the oven in stationary conditions, so they should be horizontally aligned. This is not true: the effect of the depopulation can be clearly seen in empty dots, which are computed using eq. (2.13): as the laser intensity grows up, the depopulation effect become larger and the computed density lowers. The filled dots are computed using (2.27): at high intensities, the density values are more stable. However, this second computing method has some problems at lower intensities, that are probably due to an imprecise calibration of the amplified photodiode, and it is not perfectly constant even at highest value. Moreover, as can be seen from fig. 4.5, the ratio between the peaks become smaller as intensity become bigger: this effect is not contemplated from our theory, which forecast an uniform reduction of the spectrum.

As a conclusion, the ideal situation to make density measures is when the signal is intense enough not to be almost completely absorbed (and cause saturation), but not too intense to cause depopulation (and so a density underestimation). A good way to proceed consists in setting the intensity to a low value (i.e., the attenuator

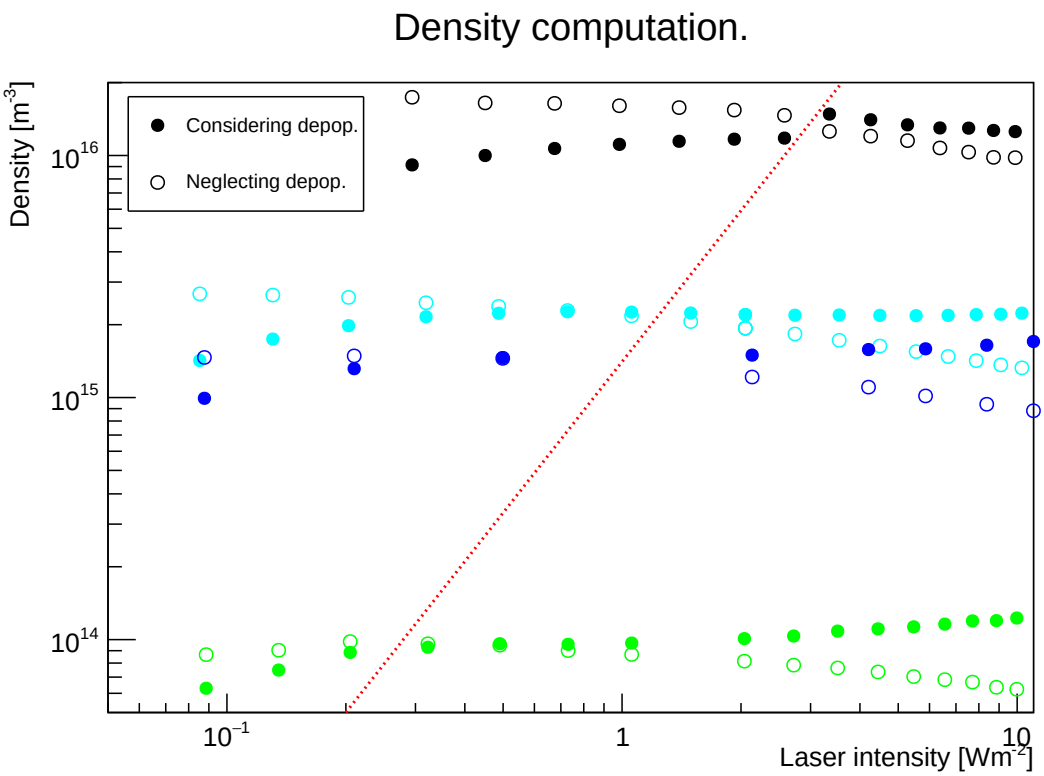

Figure 4.4: Depopulation effects at different density values. Dots of the same colour are from the same data set, i.e. with oven in stationary condition: they shall be horizontally aligned. Empty dots are computed using relation (2.13), filled ones using relation (2.27) (the error bars are smaller than the points). The red line highlight an area where depopulation and saturation effects are negligible: the system should be set to be as close as possible to this line.

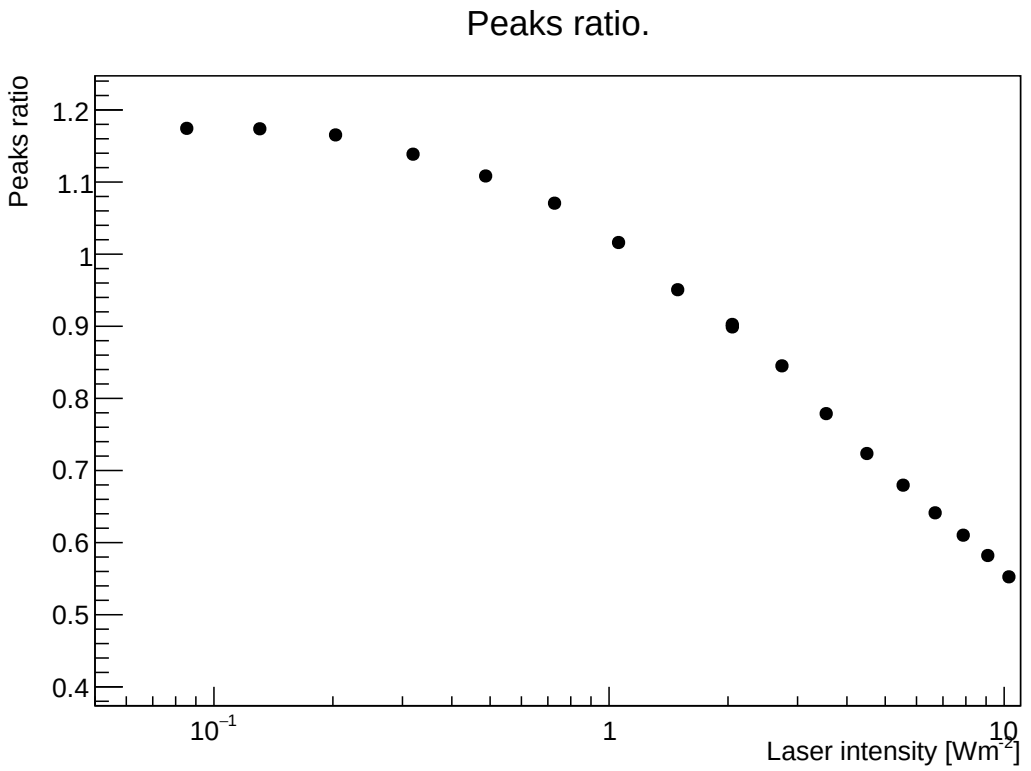

Figure 4.5: Ratio between the two peaks (defined as the integral of the Gaussians fitted on the lower-wavelength peak over the integral of the Gaussian fitted on the higher-wavelength peak).

voltage to a high value, around 3.5V) and, observing the obtained spectrum, raise up the intensity (i.e., lower the attenuator voltage) until the signal is no longer saturated; a good setting should be around the red line in fig. 4.4. The range of the density correctly measurable is therefore connected to the range of the available intensities, and consequently to the range of the variable attenuators.

Chapter 5

Oven characterization

The first purpose CATS aim to is the test and characterisation of the three SPIDER caesium ovens. Comparing the various measurements done with Laser Absorption Spectroscopy with the temperature data recorded with the thermocouples, the behaviour of each oven can be studied, reproducibility can be tested and the different ovens can be compared.

5.1 Oven Conditioning

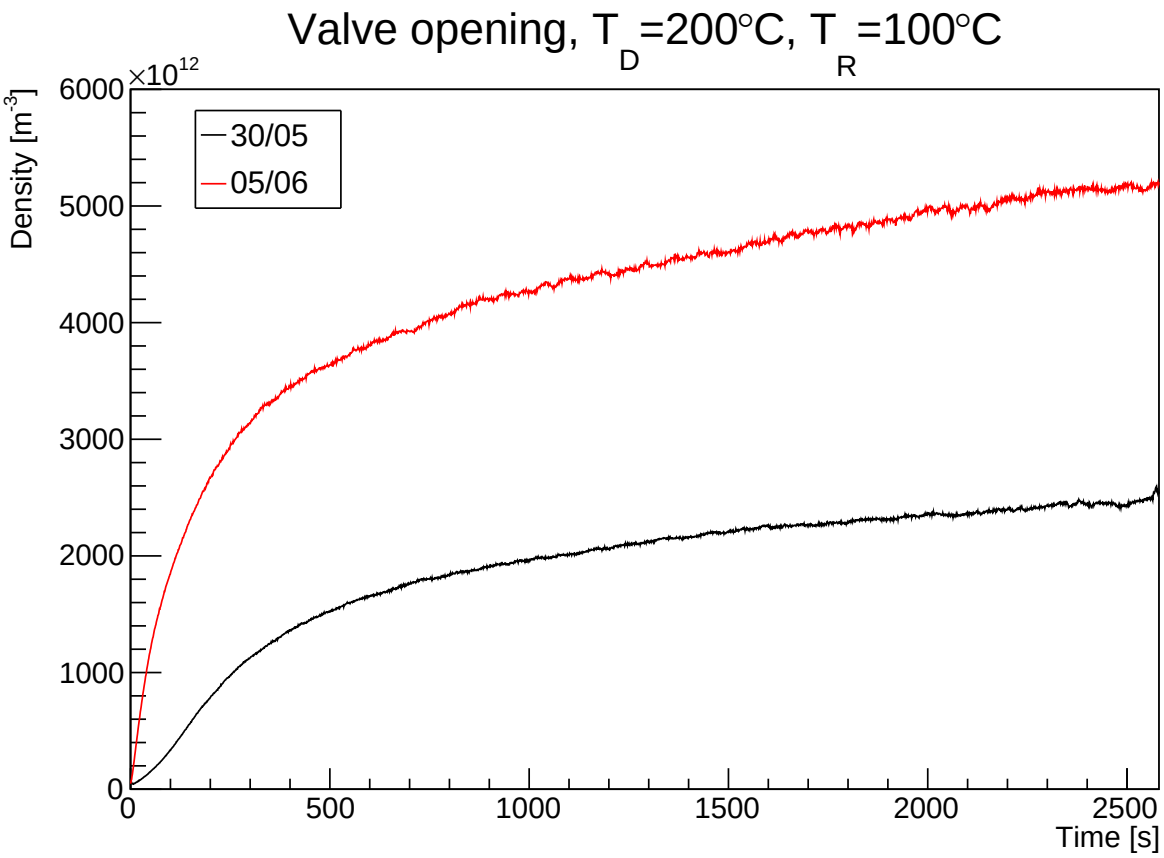

Figure 5.1: Density growth at valve opening, in same temperature condition ($T_R = 200°C, T_D = 100°C$): comparison between start and end of experimental campaign.

An important effect to be considered in the characterisation of the oven is the conditioning of the oven itself. In the first days of the experimental campaign, when the oven is heated for the first time, all the internal walls are clean. The first caesium atoms that evaporate from the reservoir find clean metallic surfaces inside the oven and settle over them. Until the oven is not completely conditioned, some caesium atoms keep settling on the internal surfaces. This results in a slower flux from the nozzle, and so in a longer time to reach the density stability. Moreover, the internal walls of the vessel have a role: caesium hitting the surfaces can both stick in the

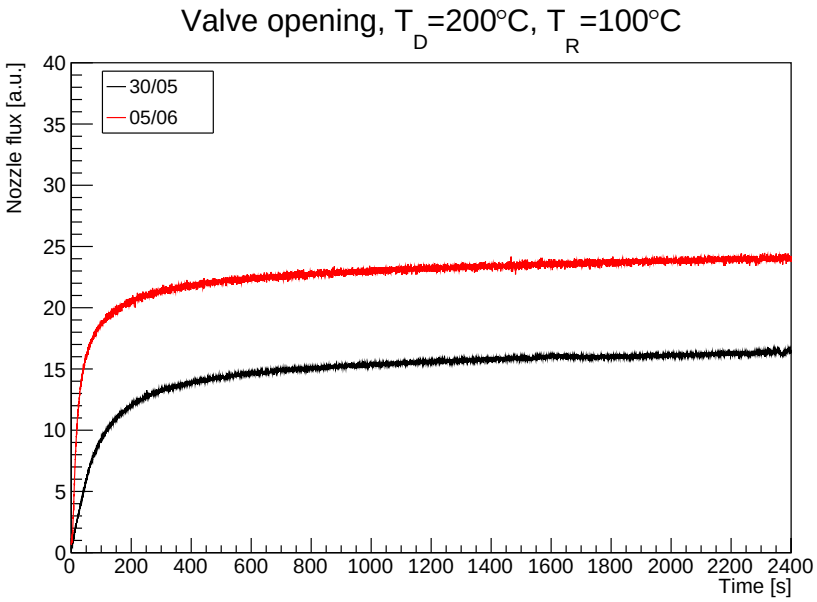

Figure 5.2: Flux around nozzle at valve opening, in same temperature condition ($T_R = 200°C, T_D = 100°C$): comparison between start and end of experimental campaign. This measurements are from another diagnostic of CATS, the SID (Surface Ionization Detector).

surface or bounce back into the vessel. This phenomena is regulated by the sticking coefficient of the walls, that from some simulations seems to be around 2% [7]: this coefficient, however, needs some time to become stable and the vessel walls are slow in conditioning. Moreover, if the oven temperature is raised, the vapour density inside the oven and the vessel grows up and so more caesium settles on the walls; oppositely when the oven temperature is lowered. This means that the first measurements done after a changing the oven temperature are way slower in reaching stability than the following ones. The oven and vessel conditioning is a slow process; this should be considered if the operative temperature of the oven is required to change frequently: to obtain a precise and stable caesium flux, the oven should be conditioned at the operative temperature before use.

To clearly see this effect, the density measure at valve opening from different days but at same temperature condition[1] can be compared (fig. 5.1): it is clear that the density growth in the first day is way slower than in the later day. LAS measurements can be compared to the SID results: the Surface Ionisation Detector is a diagnostic installed on the oven that, through a heated filament, permits the measure of a quantity proportional to the flux of caesium atoms from the nozzle [9]. As can be seen comparing fig. 5.1 (LAS measurements) and fig. 5.2 (SID measurements), the measurements from the two diagnostics are coherent in showing the acceleration of the caesium density/flux where the oven is already conditioned at the valve opening.

5.2 Temperature dependence

Some values of density are measured at different nozzle and reservoir temperatures, both with the oven 1 and the oven 2. Other measurements with the oven 3 are scheduled for the coming months.

The two thermocouples on the reservoir, TC1 and TC2, shall measure the same temperature; for the first oven, this is not true: there is a $10 - 15°C$ difference between them. On the other hand, for the second oven the two temperatures are equal. Comparing the measurements done with the two ovens and the trend of the temperature during oven heating, it was concluded that the most reliable temperature is the TC2 one (the highest one). The most probable hypothesis is that in the first oven TC1 was not perfectly placed in position, and it is a bit far from the reservoir: therefore, it measures a temperature slightly lower than the reservoir one.

The measurements are plotted in fig. 5.3. In selecting data for the plot, a particular attention has be paid to discarding data of the first day of each experimental campaign (system not yet properly conditioned), and in discarding data acquired far from the red line in fig. 4.4, i.e. when the laser intensity is not compatible with the caesium density and depopulation or saturation distort measurements. A first information that can be taken from the plot is that apparently duct temperature does not affect caesium density: there are not enough points to make an assertion, but it is a reasonable hypothesis. Secondly, the measurements from the two ovens are compatible within about 25%.

[1] To be precise, the duct temperature of the red measure is $3 - 4°C$ higher than black one (fig. 5.1): however, this temperature difference is small and can be neglected in the following argumentation.

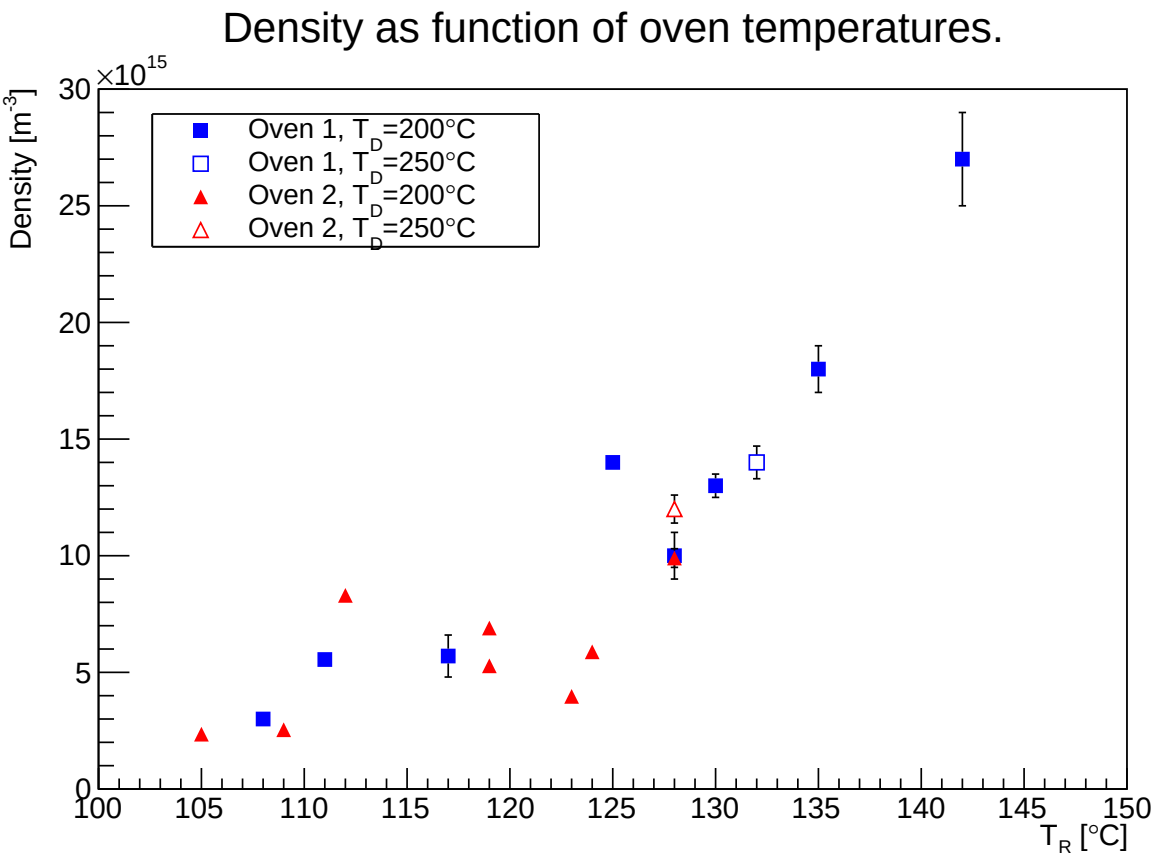

Figure 5.3: Density as function of duct and reservoir temperature, for the first two ovens. The first day of each experimental campaign (system not yet properly conditioned), as the too much saturated or depopulated signals, have been discarded.

Finally, density dependence on temperature is confirmed: as it is clear from the plot in fig. 1.6(a), as reservoir temperature increases, measured density increases itself. The Pearson r calculated on plotted data results:

$$r = 0.868179 \qquad \text{at } 16\ dof$$

This means we can reject the null hypothesis, i.e. that density and temperature are uncorrelated, with a confidence level $> 99.99\%$.

On the other hand, data are not perfectly aligned. Some differences are clear, even between measures from the same oven. This suggests that reservoir temperature is not the only parameter that controls the caesium flux from the nozzle; some other parameters, maybe linked to oven conditioning or amount of caesium in the reservoir, contribute to the caesium density.

Conclusions

LAS is a very powerful diagnostic for caesium densities: it is precise, fast, effective. On the other hand, its working range is limited by saturation and depopulation: these effects have been partially corrected but the best way to extend the observable density range is to have more flexible attenuators and a wider spectrum of laser intensities, and to avoid both saturation and depopulation.

In CATS a working LAS system has been set up, calibration has been done and analysis algorithm has been improved. With the available attenuators, more than two orders of magnitude of caesium densities have been explored. Saturation and depopulation effects have been studied: analysis algorithm parameters has been properly set and an alternative algorithm to correct depopulation has been tested. It results to be effective for small deviations, but ineffective when far from optimal conditions: in this last situation, depopulation has been proved to act in different ways in the various hyperfine levels; this means that a more complex model for depopulation must be developed to correct its effects. To prevent errors in density measurements, an optimal area where saturation and depopulation effects are negligible has been identified.

Ovens have been characterised and the density dependence on the temperature confirmed; on the other hand, it was understood that oven conditioning has a non-negligible effect on its performance. Moreover, the density-temperature relation is strongly subjected to oven conditions, so it can not be effective to provide feedback for caesium management (at least in CATS): a feedback diagnostic, such as LAS, shall be always installed[2] where caesium ovens are being operated.

[2] A LAS diagnostic system with 4 lines of sight is already planned for SPIDER

Bibliography

[1] M. Bacal and G. W. Hamilton. "H- and D- Production in Plasmas". In: *Phys. Rev. Letters* 42.1538 (1979).

[2] M. Barbisan and R. Pascqualotto. *Final report: Laser Absorption Spectroscopy diagnostic in SPIDER*. technical note RFX-SPIDER-TN-440, F4E-OFC-531-01, Task Order No.1, Deliverable D2.3 (2018).

[3] BP plc. *Statistical Review of World Energy*. 2019. URL: https://www.bp.com/content/dam/bp/business-sites/en/global/corporate/pdfs/energy-economics/statistical-review/bp-stats-review-2019-full-report.pdf.

[4] I. G. Brown. *The Physics and Technology of Ion Sources, Second Edition*. Wiley, 2004. Chap. 14.

[5] W. Demtröder. *Laser spectroscopy: basic comcepts and instrumentation*. 4th ed. Vol. 1 Chap. 2,3; Vol. 2 Chap. 2. Springer, 2008.

[6] A. S. Eddington. "The Internal Constitution of the Stars". In: *The Scientific Monthly* 11.4 (1920), pp. 297–303. ISSN: 00963771. URL: http://www.jstor.org/stable/6491.

[7] M. Fadone et al. *Interpreting the dynamic equilibrium during evaporation in a Caesium environment*. Poster ICIS 2019, paper to be published.

[8] U. Fantz and C. Wimmer. "Optimizing the laser absorption technique for quantification of caesium densities in negative hydrogen ion sources". In: *J. Phys. D: Appl. Phys.* 44.335202 (2011). DOI: https://doi.org/10.1088/0022-3727/44/33/335202.

[9] M. Fröschle et al. "Recent developments at IPP on evaporation and control of caesiumin negative ion sources". In: *Fusion Engineering and Design* 84 (2009). DOI: 10.1016/j.fusengdes.2008.12.063.

[10] R. S. Hemsworth, J.-H. Feis, et al. "Neutral beams for ITER". In: *Review of Scientific Instruments* 67.3 (1996). DOI: 10.1063/1.1146852.

[11] ITER Design Office. *The largest tokamak in the world*. 2013. URL: https://www.iter.org/album/Media/7%5C%20-%5C%20Technical.

[12] ITER Organization. *ITER website*. Accessed: 2019-08-18. URL: https://www.iter.org/mach.

[13] K.J. Lesker company. *% Trasmission of Kodial glass*. URL: https://www.lesker.com/newweb/images/product_charts/chart-hd-kodial-curve.svg.

[14] A. Kramida, Yu. Ralchenko, J. Reader, et al. *NIST Atomic Spectra Database*. National Institute of Standards and Technology, Gaithersburg, MD., 2018. URL: https://physics.nist.gov/asd.

[15] MDSplus. URL: http://www.mdsplus.org/.

[16] National Instruments. URL: http://www.ni.com/pdf/manuals/375216c.pdf.

[17] National Instruments. URL: http://www.ni.com/pdf/manuals/372101a.pdf.

[18] OSI Optoelectronics. URL: http://www.osioptoelectronics.com/Libraries/Datasheets/Photops.sflb.ashx.

[19] OZ optics. URL: https://www.ozoptics.com/ALLNEW_PDF/DTS0061.pdf.

[20] OZ optics. URL: http://www.ozoptics.com/ALLNEW_PDF/DTS0130.pdf.

[21] Sacher Lasertechnik. URL: https://www.sacher-laser.com/downloads/specifications/S2QMTg_en.pdf.

[22] B. E. A. Saleh and M. C. Teich. *Fundamentals of photonics*. Wiley, 2009. Chap. 13.

[23] D. A. Steck. *Cesium D Line Data*. 2010. URL: http://steck.us/alkalidata.

[24] Thorlabs. URL: https://www.thorlabs.com/newgrouppage9.cfm?objectgroup_id=3341.

[25] Thorlabs. URL: https://www.thorlabs.com/thorproduct.cfm?partnumber=IO-F-850APC.

[26] Thorlabs. URL: https://www.thorlabs.com/thorproduct.cfm?partnumber=V800A.

[27] Thorlabs. URL: https://www.thorlabs.com/thorproduct.cfm?partnumber=ADAFC4.

[28] Thorlabs. URL: https://www.thorlabs.com/thorproduct.cfm?partnumber=ACL108U-A.

[29] J. Wesson. *Tokamaks*. Clarendon press, 2004. Chap. 5.3.